Effect of swift heavy ion irradiation in the migration behavior of Xe implanted into TiN

H. A. Vasco[a,b], T.T. Hlatshwayo[a*], S.V. Motloung[c], M. Mlambo[a], B. S. Mwankemwa[a], S. Petrovic[d], V.A. Skuratov[e,f],

[a]Physics Department, University of Pretoria, South Africa.

[b]Department of Physics and Astronomy, Botswana International University of Science and Technology, Private Bag 16, Palapye, Botswana

[c]Department of Physics, Nelson Mandela University (NMU), P. O. Box 77000, Port Elizabeth 6031, South Africa

[d] Laboratory of Physics, Vinča Institute, Belgrade, Serbia

[e]National Research Nuclear University MEPhI, Moscow,Russia

[f]Dubna State University, Dubna, Russia

Abstract

Sintered TiN were implanted with Xe ions of 360 keV to a fluence of 1.1×10^{16} cm^{-2} at room temperature (RT) and others were co-irradiated with Xe ions of 167 MeV to a fluence of 3.4×10^{14} cm^{-2} and Xe ions of 360 keV to a fluence of 1.1×10^{16} cm^{-2} also at RT, successively. Both samples were isochronally annealed at temperatures ranging from 1100 to 1500 °C. Both irradiations caused no amorphization of the sintered TiN, however more defects were retained in the samples implanted with only Xe (360 keV) ions. Annealing of defects retained after irradiations were found to be faster in the co-irradiated samples. The migration behavior of implanted Xe was explained by trapping and de-trapping by defects at temperatures below1200 °C while at temperatures above 1200 °C, it was dominated by grain boundary diffusion, in the un-irradiated samples. In the co-irradiated samples, Xe migrated via fast grain boundaries.

Keywords: TiN; SPS; swift heavy ions; Irradiation; Raman spectroscopy.

*henryavasco@yahoo.com(H.A

1. Introduction

The generation IV gas-cooled fast reactors (GFRs) concept is proposed to combine the advantages of high temperature reactors with sustainability of fast-spectrum reactor [1,2]. These reactors are still under development with the purpose of providing power plants that are much more efficient, yet more economical and safer as compared to the Generation III reactors which are essentially an advancement of Generation II. A design of GFRs takes into account the fact that nuclear fuels will have to withstand relatively extreme aggressive operating conditions beyond those experienced in current nuclear power plants, such as high temperature and high irradiation damage induced by ions produced during fission [3,4]. Different fissile oxide, carbide and nitride such as uranium oxide/uranium, plutonium oxide (UO_2/U,Pu)O_2, uranium, plutonium carbides (U,Pu)C and uranium, plutonium nitrides (U,Pu)N are considered as alternative fuels for different nuclear reactor systems. (U,Pu)C and (U,Pu)N are being considered as suitable advanced fuels for GFRs due to their high melting temperature, high actinide density and elevated decomposition temperature and high thermal conductivity [5,6]. Nitride fuels present very desirable thermal properties such as high thermal conductivity relative to actinide oxides, high actinide density and simple phase equilibria [7]. However, a major issue confronting the use of nitride fuels is the need to enrich nitrogen into ^{15}N isotope in order to avoid production of large amounts of ^{14}C in reactor through the ^{14}N(neutron, proton)^{14}C reaction [7]. It is necessary to develop an advanced blanket/inert matrix material having resistance to aggressive conditions including both high creep strength and irradiation resistance at high temperatures. For economical purposes, the blanket/inert matrix material must be cheap, readily available and be processed at low cost. The blanket material should also possess good mechanical properties, good swelling and corrosion resistive properties. Nitride ceramics particularly titanium nitride

(TiN) is industrially used as coating film on tools for metal cutting, jet engines parts, milling and drilling tools [8,9]. It is an attractive material due to its exceptional combination of physical properties (high melting point, high hardness, low resistivity), has a metallurgical and chemical stability (high corrosion resistance to acid and alkaline solutions) [10]. It has a high wear and corrosion resistance up to reasonably high temperatures and possesses high intrinsic hardness of about 18~21 GPa [11,12]. Due to these combinations of properties, TiN is a relevant material to be used as an inert matrix in the GFRs with the intention of preventing the release of fission products.

Various sintering techniques including hot pressing, pressureless sintering and microwave sintering have been employed in sintering ceramics at different temperatures [8,9,10,13,14,15,16]. Most convectional sintering methods require high temperatures, long dwell times, and produce low relative densities of the sintered bodies [17,18,19]. Spark plasma sintering (SPS) of TiN with or without additives/cements has proven to produce desirable results when it comes to consolidation of powders [8,17]. Rapid preparation of dense ceramics with limited grain growth leading to superior mechanical properties is an added advantage for SPS [8,16].

In nuclear reactors TiN will be exposed to a lot of irradiation including ion irradiation of different energies ranging from keV to 100 MeV (the swift heavy ions (SHsI) energy regime). When SHI penetrates solid materials, most of its energy is locally deposited to the electrons and finally it can be transferred to the atoms by electron-electron and electron-atom interactions. These may result in the formation of specific radiation damage the so-called latent tracks [20]. This phenomena may results in the modification of the structure by changing the charge state of the defects or annealing due to high intense heating [21]. Under these severe conditions, TiN has

to still act as a diffusion barrier to fission products. Very limited information is available on the effect of ion irradiation in TiN and the migration behavior of different fission products [22,23,24,25]. For TiN to be used as matrix material of GFRs, the influence of irradiation in the migration behavior of important fission products need to be understood. Xenon is one of the abundant fission products [24]. Due to the importance of Xe, the migration behavior in TiN has been investigated [13,24,25]. However, the influence of irradiation in the migration behavior of Xe in TiN has not been reported. Thus, in this study, we report on the effect of SHI on the migration of Xe in sintered TiN. The results of this study are important in understanding the behavior of TiN in conditions similar to the nuclear reactor environments.

2. Experimental procedures

TiN powder of 99 % purity supplied by Sigma was sintered into 20 mm diameter samples using spark plasma sintering (SPS) at Tshwane University of Technology Pretoria, South Africa. The sintering process was conducted at a temperature of 1900 °C in a vacuum of 100 mbar under

50 MPa maximum pressure. The heating rate was 100 °C/min and the holding time at maximum temperature was 10 min.

The Density of the sintered samples were determined by the liquid displacement method in deionized water (Archimedes' principle). The sintered samples were cut into 10×10 mm^2 using a diamond saw. The cut samples were then polished to 0.25 µm using diamond suspension to remove scratch marks from cutting process. The as-polished samples were then successively cleaned using acetone, deionised water and methanol.

Some of the polished samples were implanted with Xe ions of 360 keV at room temperature to a fluence of 1.1×10^{16} cm^{-2} (Xe-360 keV) and others were firstly irradiated with Xe ions of 167

MeV to a fluence of 3.4×10^{14} cm^{-2} followed by Xe ions of 360 keV to 1.1×10^{16} cm^{-2} (Xe-360 keV+167 MeV). All irradiations were performed at room temperature. . Fig. 1 shows the schematic diagrams of implantation and irradiation processes, their respective current intensities are indicated. High flounces were chosen to maximize radiation damage retained after both irradiations. The low energy ions irradiations were performed at Vinća institute, Serbia and the high energy irradiations were performed using the IC-100 cyclotron at Flerov Laboratory for Nuclear Reactions (FLNR), Joint Institute for Nuclear Research (JINR) in Dubna, Russia

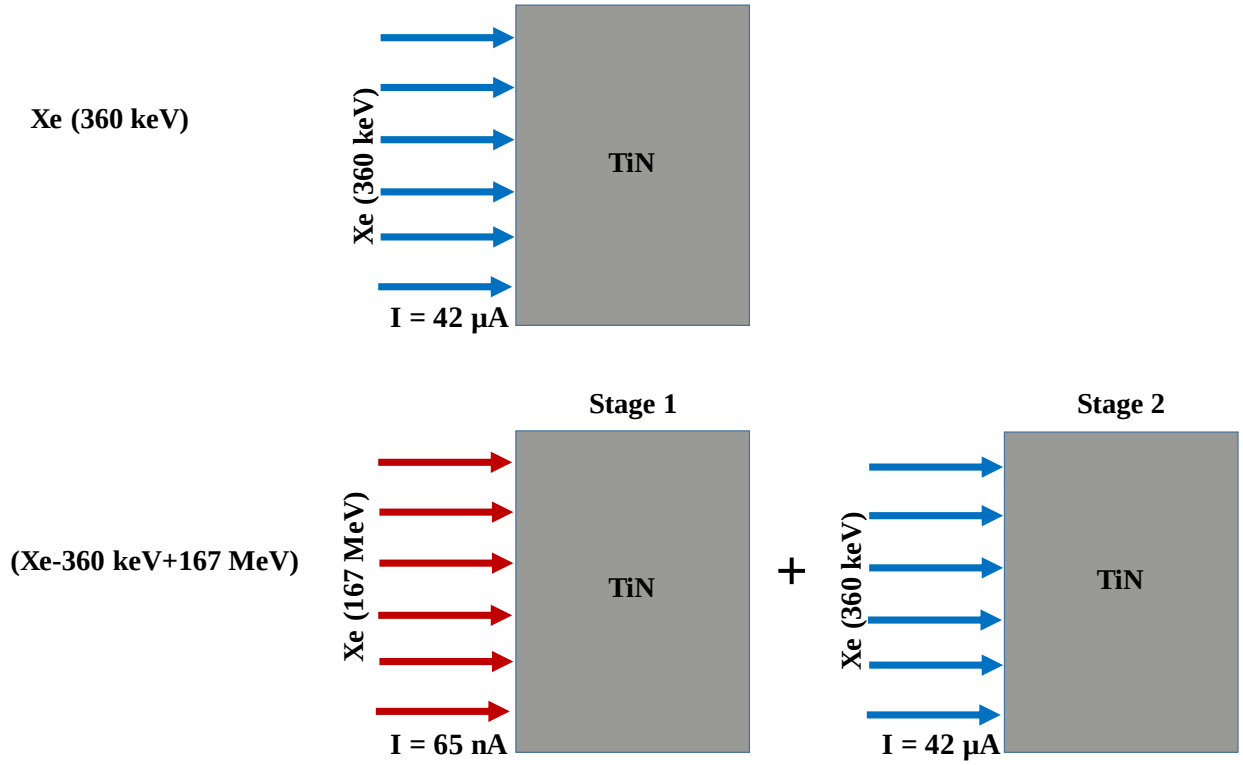

Fig. 1: Schematic diagrams of irradiations.

Fig 2 shows the simulated profiles of Xe ions of 167 MeV irradiated into TiN and Xe ions of 360 keV implanted into TiN. From these profiles, it is quite clear that irradiation with Xe ions of 167 MeV resulted in electronic energy loss from the surface to about 10 µm and the ions come to rest at projected range of 9.11 µm while implantation of Xe ions of 360 keV resulted in the

nuclear energy loss from the surface to about 120 nm .and the ions come to rest at about 72.7 nm. Since the Xe ions of 167 MeV irradiation was performed before implantation the interaction of point defects retained by swift heavy ions irradiation and defects caused by implantation is expected. Therefore, the influence of these interactions in the migration of implanted Xe (slow moving ions) is expected in the Xe-360 keV+167 MeV samples.

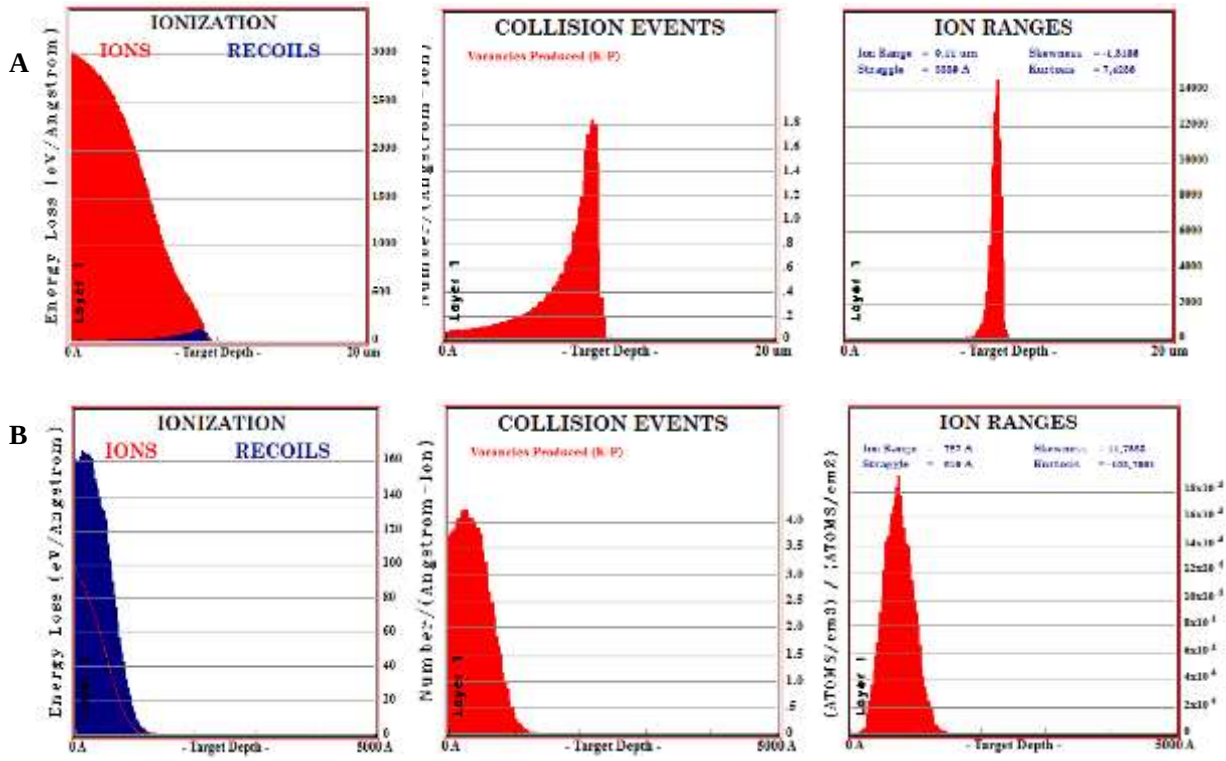

Fig. 2: SRIM simulated profiles of Xe ions (of 167 MeV (a) and 360 keV (b)) irradiated into TiN.

Both the Xe-360 keV and Xe-360 keV+167 MeV samples were isochronal annealed for 5 hours in the temperature ranging from 1100 to 1500 °C in steps of 100 °C under vacuum using a computer controlled Webb 77 graphite furnace.

The prepared samples were characterized by Raman spectroscopy (RS), scanning electron microscopy (SEM) and X-ray photoelectron spectroscopy (XPS) and Rutherford backscattering spectrometry (RBS). RS spectra were recorded with a T64000 series II triple spectrometer

system from HORIBA scientific, Jobin Yvon Technology, using the 514.3 nm laser line of a coherent Innova® 70C series Ar^+ laser (spot size ~ 2 mm) at power of 0.17 mW with a resolution of 2 cm^{-1}. The surface morphologies were monitored by an in-lens detector using an acceleration voltage of 2.0 kV using a Zeiss Ultra Plus field emission scanning electron microscope (FE-SEM, ZEISS SEM MICORSCOPES Cross beam 540). X-ray photoelectron spectroscopy (XPS) surface analysis of the sintered samples was done using the Thermo SCIENTIFIC K- Alpha X-ray photoelectron spectrometer with monochromatic Al-Kα radiation. Rutherford backscattering spectroscopy (RBS) at RT was performed using He^+ particles with energy of 1.6 MeV at a backscattering angle of 165°. The beam current was kept at 10 nA. For better statistics, 8 μC was collected per measurements. The Xe RBS profiles in energy-channels were converted into depth profiles (in nm) using energy loss data. The theoretical density of 5.39 gcm^{-3} was used.

3. Characterization of sintered TiN

The Raman spectrum of as sintered TiN is shown in Fig. 3, it consists of bands at 236, 321, 445 and 557 cm^{-1}. The two peaks at 236, 321 cm^{-1} are due to the first order scattering corresponding to the acoustic transitions (transverse, TA and longitudinal acoustic, LA). These acoustic scattering bands are attributed to the vibrations of the Ti atoms [26]. The bands between 350 and 700 cm^{-1} are due to nitrogen ions. The band at 445 cm^{-1} is assigned to TiO_2 [27]. The broad band at 557 cm^{-1} is assigned to the optical mode attributed to the vibration of the N atoms. TiN is known to assume NaCl structure face-centered cubic (fcc) and to undergoes octahedral symmetry (O_h). In its perfect crystals only the zone center phonons can be Raman active, and usually not even all of them. The selection rules for Raman do not allow O_h symmetry, therefore first order scattering is forbidden in TiN [26]. Although first order is forbidden in TiN, the presence of defects in TiN results to the detection of the first order scattering. The presence of the TiO_2 is

attributed to oxidation of the TiN. To confirm the oxidation of TiN, the Raman spectrum was fitted using Gaussian– Lorentzian. The Raman spectrum fitted well with five peaks at 236, 321, 442, 557 and 614 cm^{-1}. A broad peak around 236 cm^{-1} is due to TA mode, and a narrow peak at 320 cm^{-1} confirmed the LA mode. A fairly weak peak at 451 cm^{-1} assigned to TiO_2 was observed around 442 cm^{-1} confirming oxidation. The broad peak due to optical mode (TO) of sintered TiN is observed at 557 cm^{-1}. The deconvolution of this peak revealed two peaks at 557 and 614 cm^{-1}. The second peak at 614 cm^{-1} is attributed to the optical mode of the TiO_2 phase [27].

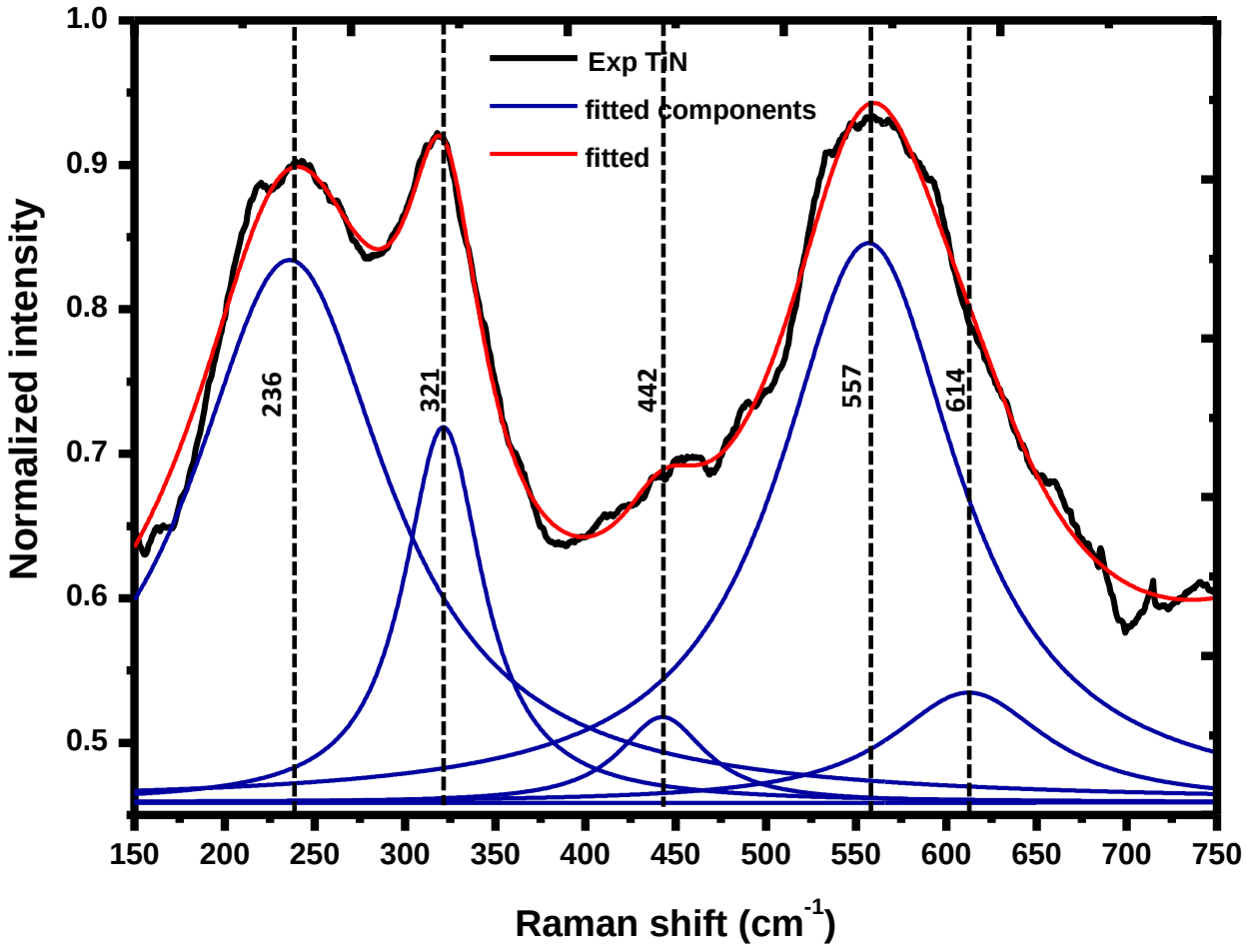

Fig. 3: Raman spectrum of sintered TiN, fitted and fitted components (Lorentzian- Gaussian).

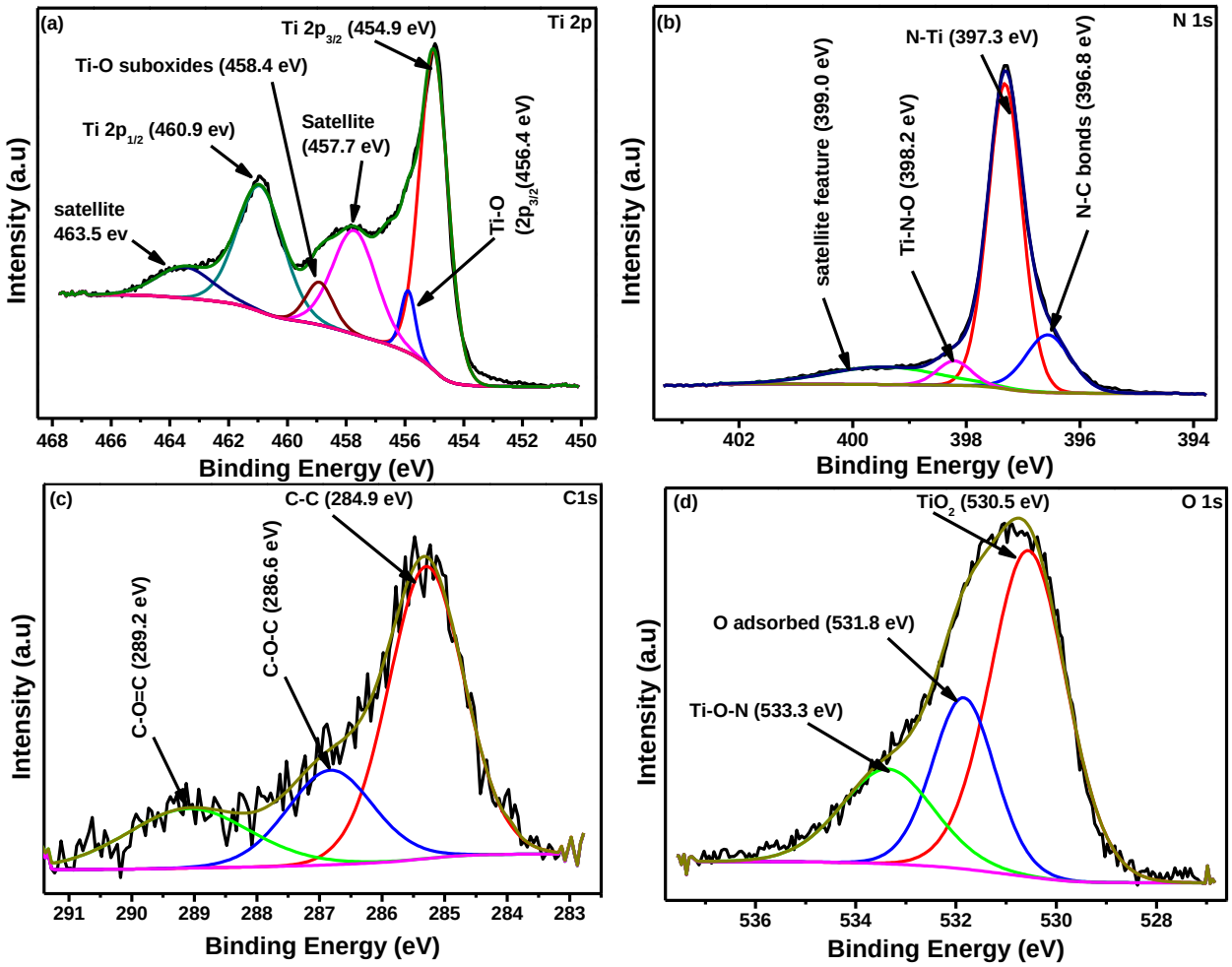

Fig. 4: The high resolution XPS spectra of (a) Ti 2p, (b)N 1s, (c) C 1s and (d) O 1s.

In order to gain more insight into the composition and chemical states of the sintered TiN, XPS was performed on the samples. High resolution XPS spectrum for Ti 2p as shown in Fig. 4 (a) displayed Ti $2p_{3/2}$ and Ti $2p_{1/2}$ positioned at binding energies of 454.9 and 460.9 eV, respectively consistent to the Ti – N bonds in TiN. The spin-orbit difference between the Ti 2p doublets was 6.0 eV which revealed that the bonding state of Ti is in the form of TiN [28]. The deconvoluted TiN spectrum showed a peak located at binding energy of 456.4 eV corresponding to the Ti-O bonds and a peak at 458.4 eV may be attributed to the sub-oxides of TiO_2 [28,29]. This indicates that the surface of the samples were oxidized. The observed satellite peaks at binding energy

~2.7 eV higher than the Ti 2p3/2 and Ti 2p1/2 peaks differentiates TiN from TiO_2. Fig. 4 (b) shows N 1s high resolution spectrum deconvoluted by using Gaussian fit into three components located at 396.8, 397.3 and 398.2 eV. The first component from the low binding energy side (396.8 eV) could be attributed to surface carbon-nitrides (N-C) bonds [29]. The main peak at 397.3 eV was assigned to the N bonded Ti forming TiN [28,30]. The peak at 398.2 eV originates from titanium oxynitrides and the relatively low intense component centred at 399 eV is due to the presence of the free nitrogen at the interstitial sites [28,31]. Fig. 4 (c) shows the spectrum of C1s with a prominent peak at 284.9 eV which could be attributed to C-C. The remaining two peaks at 286.6 and 289.2 eV were attributed to adventitious peaks of C-O-C bond and C-O=C, respectively [32]. There is a possibility of adventitious carbon and oxygen contaminated the samples as were prepared and stored in an open environment. O1s core level photoelectron was fitted into three different fragments as shown in Fig. 4 (d). The first component at 530.5 eV is ascribed to TiO_2, the second component at 531.8 eV is assigned as the elemental O (or physically adsorbed molecular H_2O) and the third component at 533.3 eV is identified to be originated from Ti-O-N phase [32]. These results are in agreement with Raman results which also indicated the oxidation of the samples surfaces.

The SEM image of the as-sintered TiN is shown in Fig. 5. There are a few marks running across the sample surface, they could have been created during polishing. There are few pores observed, confirming the densification of TiN powder without any additives, and 98.5 % relative density was achieved as confirmed by Archimedes' principle.

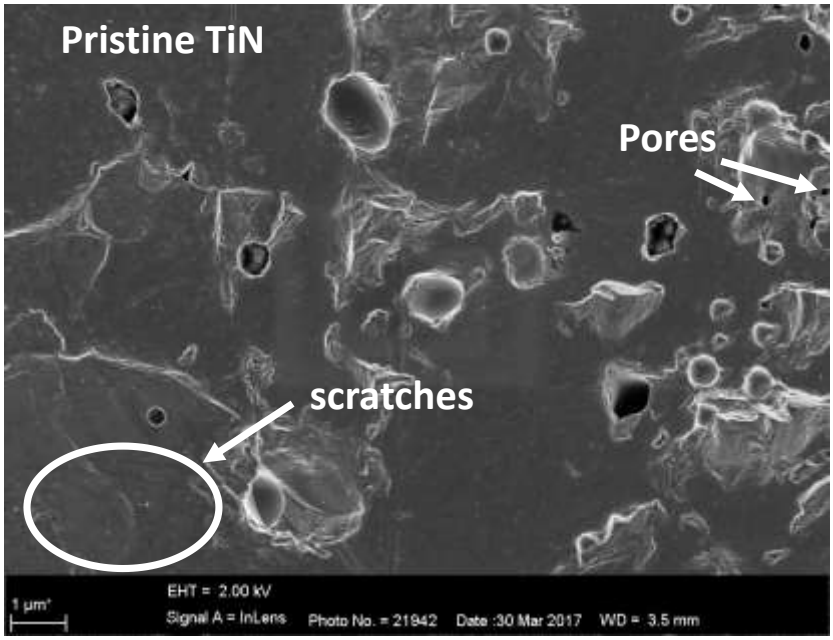

Fig. 5: The SEM image of as-sintered TiN.

4. Results and discussion

4.1 Irradiation of TiN

Raman spectra of Xe-360 keV and Xe-360 keV+167 MeV samples compared with the Raman spectrum of pristine TiN (Virgin) are shown in Fig 6. No amorphization was observed in both Xe-360 keV and Xe-360 keV+167 MeV as can be seen in Fig. 6 that the specimens retained most of the original main peaks as observed relative to the pristine sample.

The sample implanted at room temperature with Xe 360-keV resulted to a slight combination of the peaks 200 to 350 cm^{-1} region. The broadening of the optical band was observed. These indicated that some radiation damage was retained after irradiation. The co-irradiated sample Xe-360 keV+167 MeV revealed similar peak combination of the acoustic bands and broadening of optical band. To get more insight on the radiation damage retained in both samples, the Raman spectra of both samples were deconvoluted.

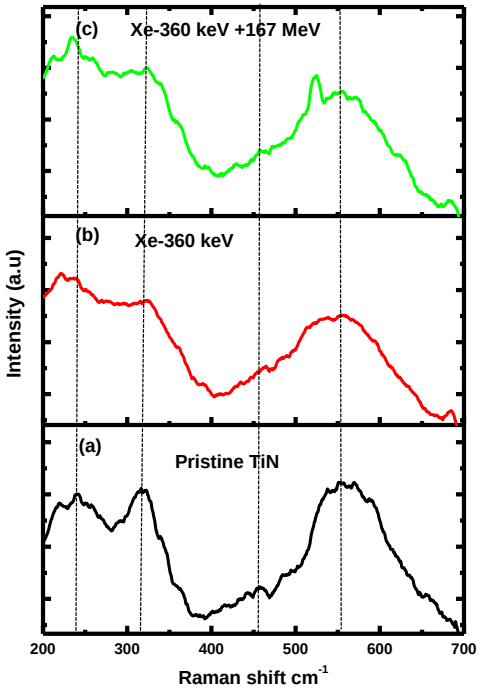

Fig. 6: The Raman spectra of TiN implanted with Xe of 360 keV to a fluence of 1.1×10^{16} cm^{-2}at RT (Xe-360 keV) and co-irradiated with Xe of 167 MeV to a fluence of 3.4×10^{14} cm^{-2} and with Xe ions of 360 keV to a fluence of 1.1×10^{16} cm^{-2}respectively (Xe-360 keV+167 MeV), all at RT. The Raman spectrum for pristine TiN is included for comparison.

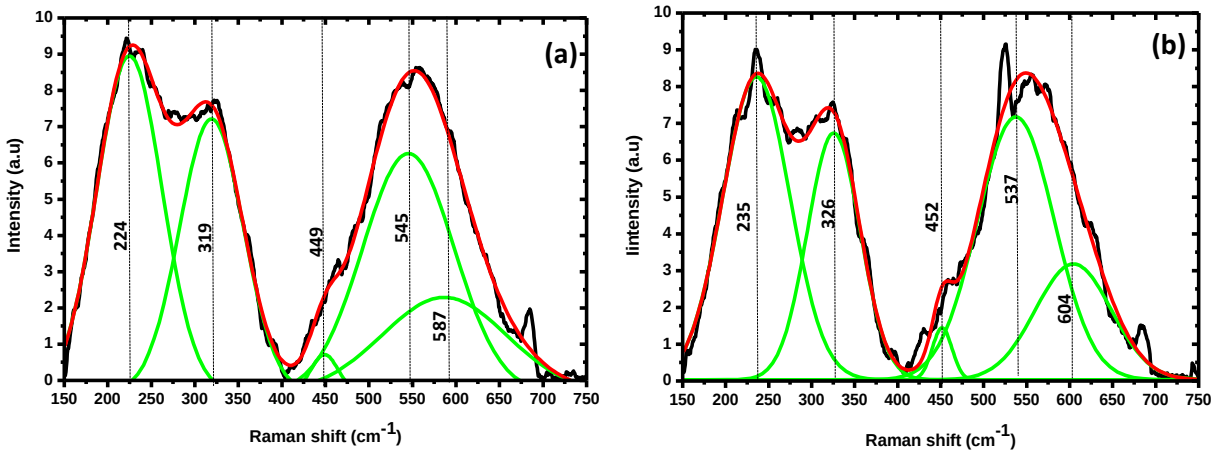

Fig. 7: (a) The Raman spectrum of sintered TiN implanted with Xe-360 keV to a fluence of 1.1×10^{16} cm^{-2} at RT, fitted and fitted components (Lorentzian- Gaussian) and (b) The Raman spectrum of sintered TiN co-irradiated with

Xe-360keV + 167 MeV to a fluence of 1.1×10^{16} and 3.4×10^{14} cm^{-2}respectively at RT, fitted and fitted components (Lorentzian- Gaussian)

Fig. 7 (a) shows the deconvoluted Raman spectrum of sintered TiN implanted with Xe-360 keV to a fluence of 1.1×10^{16} cm^{-2} at RT. The spectrum reveals that the TA mode has shifted from 236 to 224 cm^{-1}, LA mode shows a very insignificant shift from 321 to 319 cm^{-1}, while the TiO_2 peak shifted to 449 cm^{-1}. The optical mode also reveals a shift from 557 to 545 cm^{-1}. The oxide shoulder which was observed at 614 cm^{-1} in the pristine samples has shifted to 587 cm^{-1}. Fig. 7 (b) shows the deconvoluted Raman spectrum of sintered TiN co-irradiated with Xe-360keV and 167 MeV to a fluence of 1.1×10^{16} cm^{-2} and 3.4×10^{14} cm^{-2} respectively at RT. The TA mode revealed no significant shift with respect to the pristine samples, while the LA mode showed a shift to larger wavenumbers, from 321 to 326 cm^{-1}. The TiO_2 peak shifted from 442 to 452 cm^{-1}. The optical mode shifted from 557 to 537 cm^{-1}, while a TiO_2 peak at 614 shifted 604 cm^{-1}. These differences in peak shifts either to lower or higher wavenumbers indicate the different stress caused after single and dual irradiation. The full with at half maximum (FWHM) of the TO peaks were calculated from the deconvoluted spectra. They were found to be 91, 125 and 105 for pristine, Xe-360 keV, and Xe-360 keV+167 MeV samples, respectively. The broadening of the TO peak indicates the relative amount of radiation damage retained. Therefore, more defects/damages were retained in Xe-360 keV compared to Xe-360 keV+167 MeV. The different amount of damage retained in Xe-360 keV and Xe-360 keV+167 MeV samples might be due to the interaction of defects in the latter. Generally, these results indicate that irradiating with slow moving ions and co-irradiating with both slow and swift heavy ions did not caused severe radiation damage in TiN. Similar radiation tolerance have been reported in TiN for slow moving ions [33].

The SEM images of Xe-360keV and Xe-360 keV+167 MeV samples are shown in Fig. 8, the SEM image of pristine TiN included for comparison. The Xe-360keV sample in Fig. 6 shows very few pores and generally it does not look any different from the pristine sample. The Xe-360 keV+ 167 MeV samples have bigger crystals (similar to the ones observed in Xe-360keV samples), some finer crystals of different sizes also appeared on the surfaces. The difference might be due to localised heat during SHI irradiation before annealing or interaction of defect retained after SHI irradiation and the ones produced during slow ions irradiation. More investigations are required to clarify this.

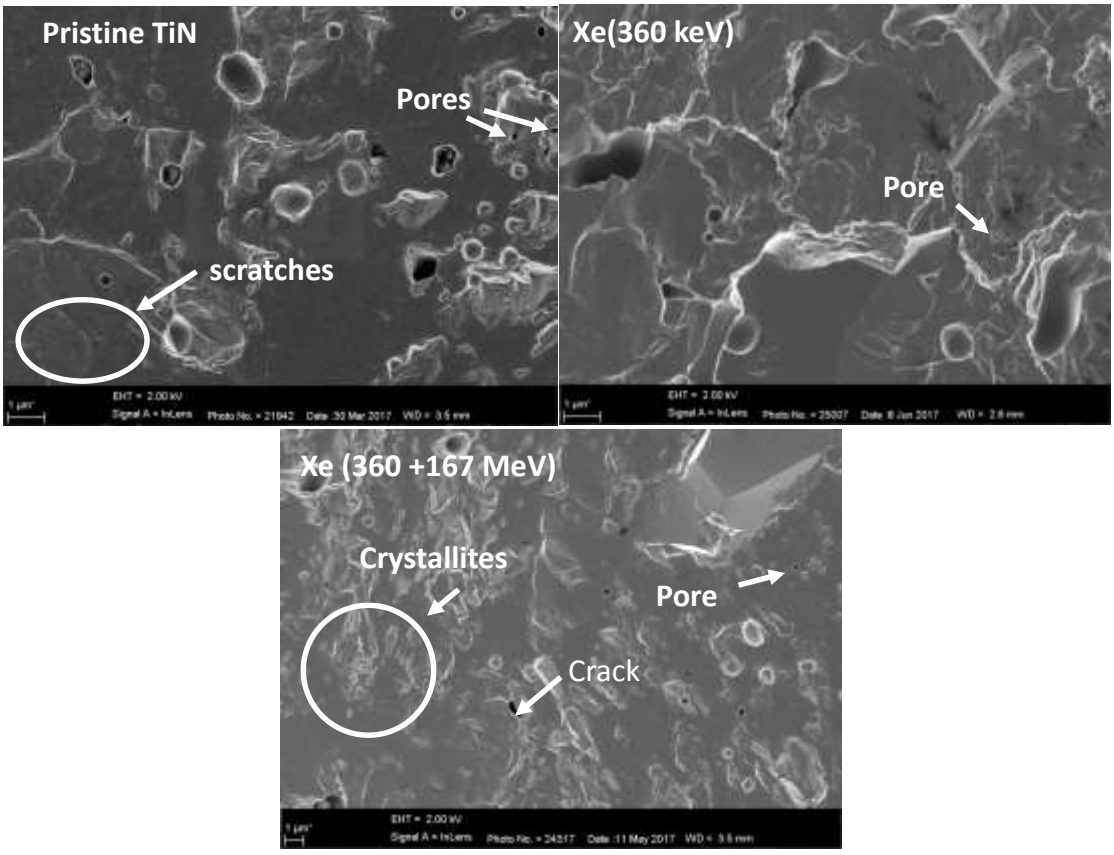

Fig. 8: The SEM images of the Pristine TiN, TiN implanted with Xe of 360 keV to a fluence of 1.1×10^{16} cm^{-2}at room temperature (Xe-360 keV) and co-irradiated with Xe of 167 MeV to a fluence of 3.4×10^{14} cm^{-2} and implanted with Xe ions of 360 keV to a fluence of 1.1×10^{16} cm^{-2}respectively (Xe-360 keV+167 MeV).

5. Annealing results

Both Xe-360 keV and Xe-360 keV+167 MeV samples were isochronally annealed at temperatures ranging from 1100 to 1500 °C in steps of 100 °C for 5 hours. Their Raman spectra are presented in Fig. 9, with pristine TiN, un-annealed Xe-360 keV and Xe-360 keV +167 MeV spectra included for comparison. After annealing Xe-360 keV samples at 1100 °C, a further slight combination of TA and LA mode was observed. This was accompanied by a blue-shift of the TO mode to 533 cm^{-1} and narrowing compared to the implanted and pristine samples. The shift was attributed to stress due to implanted Xe while slight combination of TA and LA mode together with narrowing indicated the reduction of the defects. As the annealing temperature was increased from 1200 to 1500 °C, more annealing of the defects was observed with TA and LA mode combining, while the TO mode remaining at 533 cm^{-1} compared to the pristine TiN with the increase in annealing temperature. After annealing at 1300 °C, a new peak attributed to LO mode of TiN in the region between 600 to 700 cm^{-1} emerged. This peak became more prominent as the annealing temperature was increased up to 1500 cm^{-1}. The LO mode was clearly observable at 630 cm^{-1} after the annealing temperature of 1500 °C.

The Xe-360 keV +167 MeV revealed similar behaviour as Xe-360 keV samples after annealing at 1100 °C, with TA and LA peaks combining and narrowing of the TO mode (which shifted to 536 cm^{-1}). The other noticeable feature was the appearing of LO mode at 635 cm^{-1} after annealing at this annealing temperature (1100 °C). As the annealing temperature was increase from 1200 to 1500 °C, a combination of TA and LA mode was further observed while the TO mode remained in the same region of 536 cm^{-1} with LO mode becoming more pronounced above 600 cm^{-1}. Comparing this result with that of Xe-360 keV (which showed no LO mode) after

annealing at the same temperature (1100 °C), suggests faster annealing of defects in the Xe-360 keV +167 MeV samples.

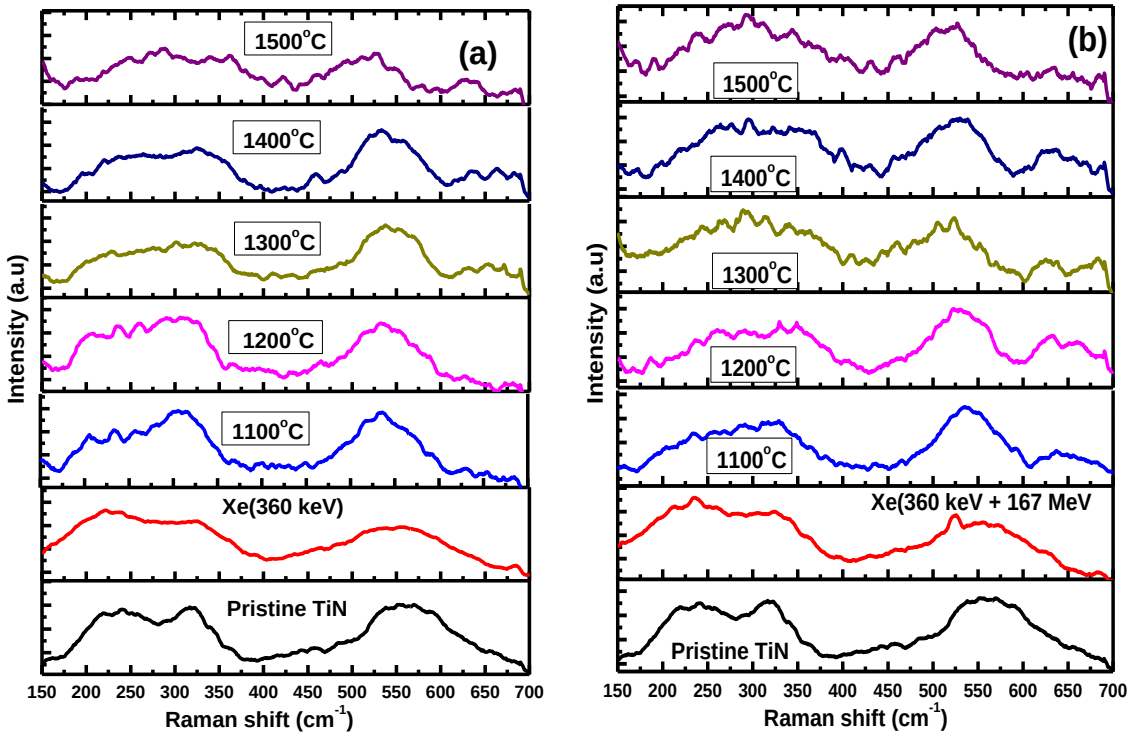

Fig. 9: The Raman spectra of Xe-360 KeV (a) and Xe-360 KeV +167 MeV (b) TiN after being isochronally being annealed at different temperatures from 1000 °C to 1500 °C at 5hour cycles. The Raman spectrum of the pristine TiN is included for comparison.

The evolution of the morphology and topology of the samples was investigated after each isochronal annealing cycle from 1100 to 1500 °C. The results are shown in Fig. 10. After annealing at 1100 °C the Xe-360 keV samples did not show much change on the surface as compared to the un-annealed samples. At elevated annealing temperatures the surface became smoother and less distinct grain boundaries appeared. Annealing the Xe-360 keV+167 MeV samples at 1100 °C also caused some smoothening of the surfaces and some more distinct grain boundaries with crystallites forming along their interface appearing on the surface. As the annealing temperature was increased the number of grain boundaries also increased which is

similar to the results reported by Bes' *et al* [13]. In contrary to what Bes' *et al* [25], there were no bubbles observed in both samples after annealing. The difference in surfaces features after annealing might be due to different annealing of defect after annealing at different temperatures as observed in Raman results.

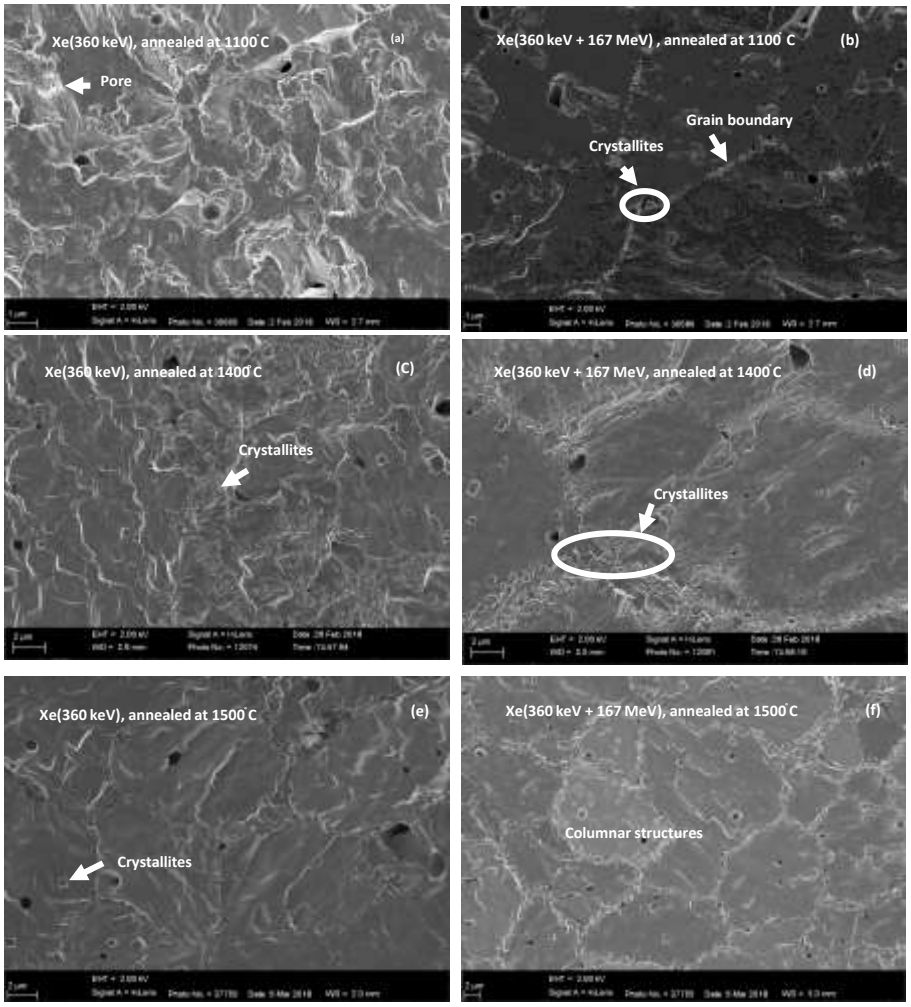

Fig. 10: SEM images of Xe-360 keV and Xe-360 keV+167 MeV after being subsequently annealed at (a) 1100, (1200, 1300, not shown here), 1400 °C, 1500 °C.

In the Xe-360 keV+ 167 MeV samples, the slow ions were implanted in an already defective TiN. The pre-existing defects interacted with the defects caused by implantation which resulted into the formation of new defects. In the Xe-360 KeV, the implantation was performed in a virgin

TiN and defects were created by implantation. Annealing these samples at 1100 °C caused faster annealing of defects in the Xe-360 keV+ 167 MeV samples compare to Xe-360 KeV as was observed in the Raman results (Fig. 9). The bigger crystals in Xe-360 keV+ 167 MeV samples might be due to relatively faster annealing of the defects in these samples.

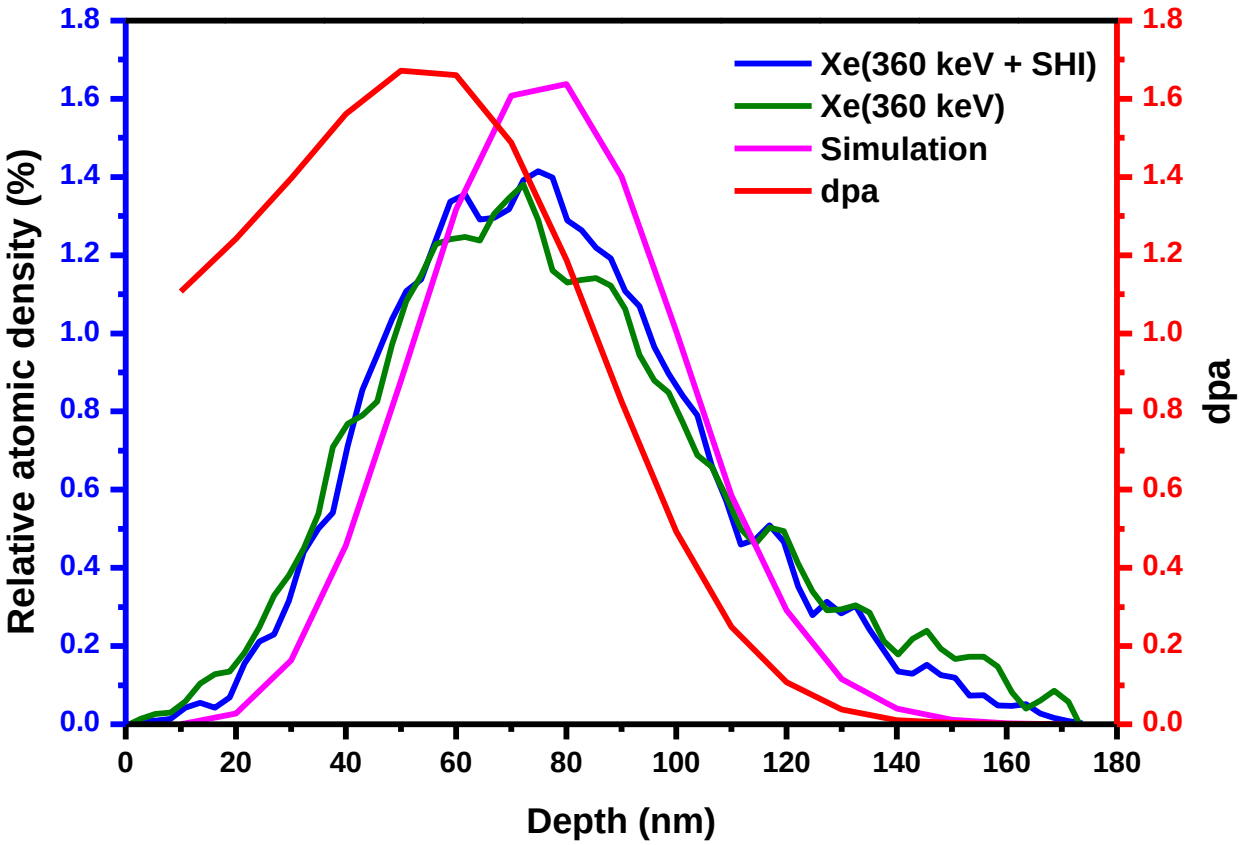

Fig. 11: Depth profiles of Xe (360 keV) implanted into TiN at room temperature to a fluence of 1×1016 cm^{-2} (Xe-360 keV), Xe (360 keV) impanted into TiN(pre irradiated with Xe (167 MeV) to a fluence of 3.4×10^{14} cm^{-2}at room temperature) to 1.1×10^{16} cm^{-2} at room temperature and TRIM simulated Xe of 360 keV in TiN(simulation). The simulated damage in displacement per atom (dpa) is included.

Fig. 11 shows the depth profiles of Xe implanted into TiN for Xe-360 keV and Xe-360 KeV +167 MeV samples as compared with SRIM simulation. The simulated damage in displacement per atom (dpa) are also included in Fig. 9. The ion fluence was converted into dpa using [33]:

$$dpa = \frac{\frac{Vac}{ionÅ} \times 10^8}{\rho_{TiN}(atoms^{-3})} \times \varphi(ions^{-2})$$

where φ the ion fluence, ρ_{TiN} is the theoretical density of TiN (5.39 g/cm^3) and $\frac{Vac}{ionÅ}$ is the vacancy per ion ratio from SRIM 2012 [34]. The measured Xe depth profiles are slightly broader but in reasonably agreement with SRIM simulation. From these results, it is quite clear that SHI irradiation prior to implantation had insignificant effect on the distribution of implanted Xe. The retained damage are more towards the surface as compared to the implanted Xe profiles.

The Xe depth profiles of Xe-360 keV and Xe-360 KeV +167 MeV samples after sequential annealing at temperatures from 1100 to 1500℃ in steps of 100 °C for 5 hours together with their Xe retain ratio and square of FWMs as function of temperature are depicted in Fig. 12 and 13, respectively. Annealing the 360-keV at 1100 °C caused a shift of Xe peak towards the bulk .This shift was not accompanied by neither broadening nor loss of of the implanted Xe. These results indicate the lack of Fickean diffusion after annealing at this temperature. Annealing at 1200 °C caused a peak shift towards the surface resulting in the Xe peak returning to its original position. This was accompanied by slightly broadening of the Xe peak (indicating Fickean diffusion) and 20% loss of implanted Xe. Neither further broadening of Xe peak nor shift was observed after annealing at 1300 °C, however about 40 % of the implanted Xe was lost. A significant peak shift towards the surface was observed after annealing at 1400 ˚C. This was accompanied by 60 % loss of Xe from the surface. These resulted in the surface side of the Xe profile at this temperature (1400°C) to be truncated which indicated the direct release of Xe as it reaches the surface. This shift towards the surface resulted in the subsequent loss of almost all the Xe after annealing at 1500 °C. No signs of thermal etching were observed during SEM analysis of the annealed samples-Fig.10.

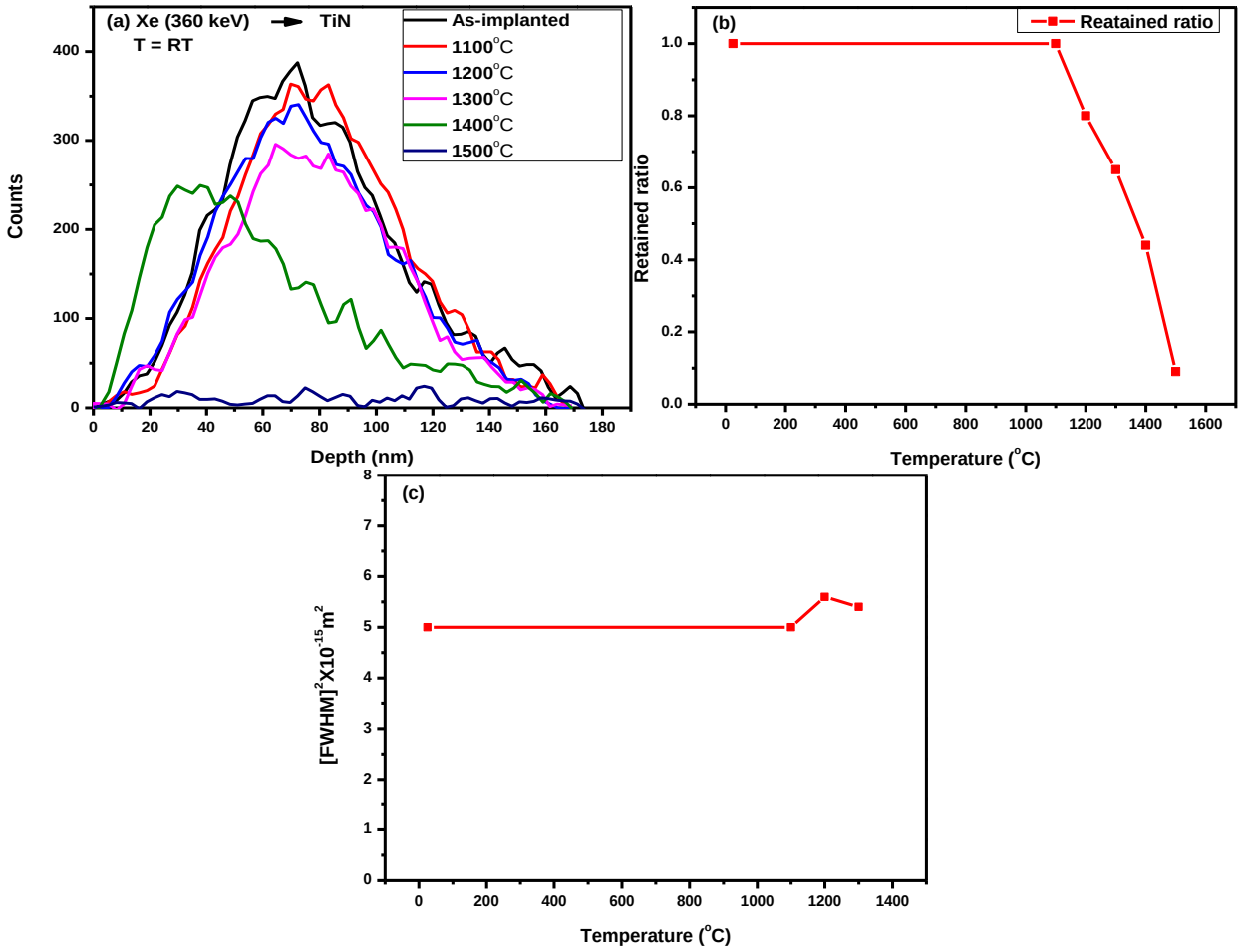

Fig. 12: (a) The depth profiles of Xe (360 keV) implanted into TiN to a fluence of 1.1×1016 cm^{-2} at room temperature (RT) after isochronal annealing at temperatures at from 1100 to 1500 °C for 5hours, the as-implanted Xe depth profile is included for comparison ,(b) the retained ratio of Xe (c) Square of Full width at half maximums (FWHMs) as function of temperature.

Unlike in the Xe-360 keV samples, no change was observed in the implanted Xe after annealing the Xe-360 KeV +167 MeV samples at 1100 ºC-Fig 13. About 15% was lost after annealing at 1200 ºC. This loss was accompanied by peak broadening and shift. This loss without peak broadening and shift became significant with annealing temperature resulting in the total loss of implanted Xe at 1500 °C. These results indicate the lack of Fickean diffusion in the Xe-360 KeV +167 MeV samples

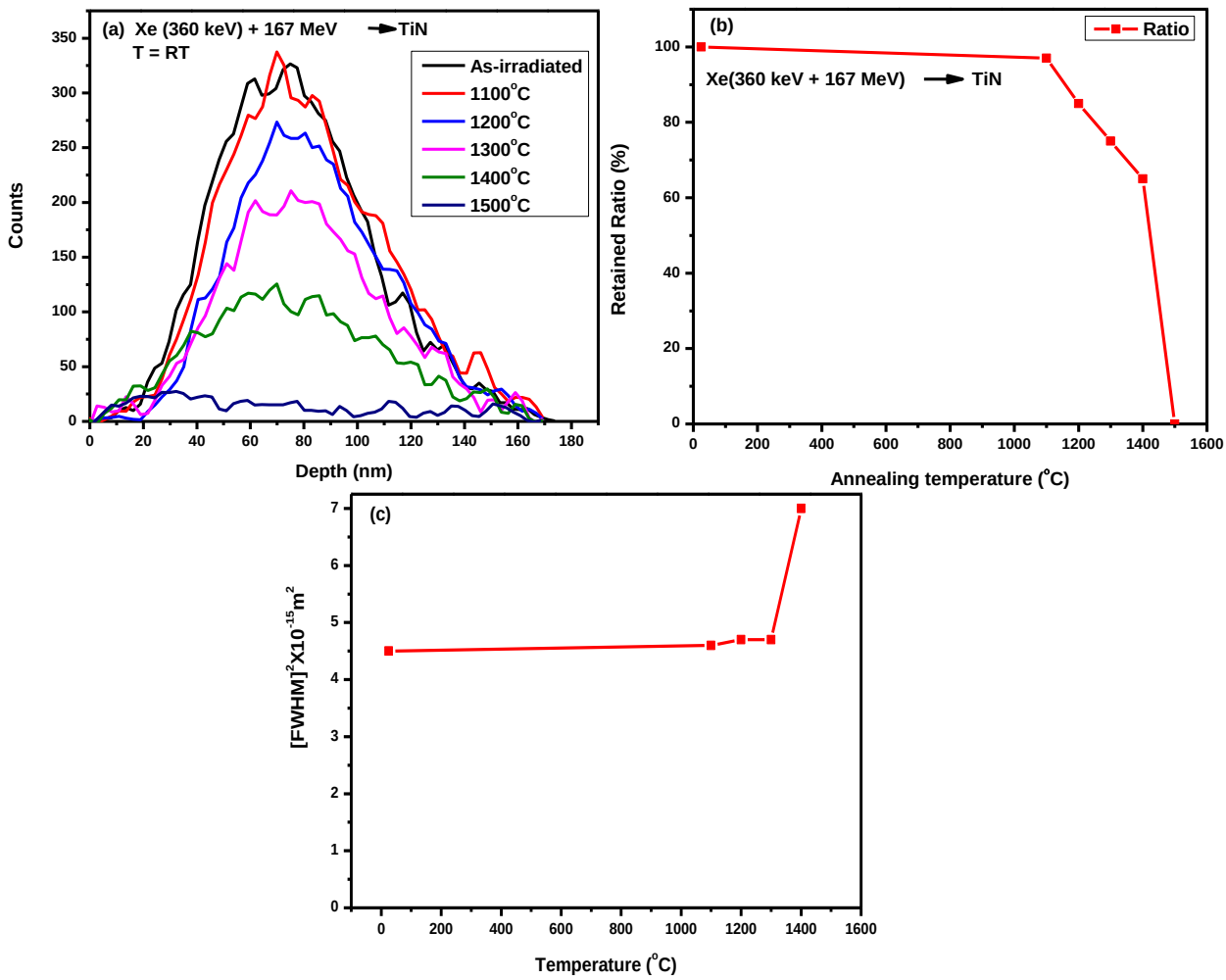

Fig. 13. (a) (a) The depth profiles of Xe (360 keV) implanted into TiN (pre irradiated with Xe (167 MeV)) to a fluence of 1.1×10^{16} cm^{-2} at room temperature (RT) after isochronal annealing at temperatures at from 1100 to 1500 °C for 5hours, the as-implanted Xe depth profile is included for comparison ,(b) the retained ratio of Xe (c) Square of Full width at half maximums (FWHMs) as function of temperature.

Comparing these results, it is quite clear that the migration behaviour of Xe in the Xe-360 keV and Xe-360 KeV +167 MeV samples is totally different. The different behaviour might be due to different radiation damage retained in both samples and their annealing resulting different structures. After annealing at 1100 °C, Raman results indicated more annealing of defects in the Xe-360 KeV +167 MeV samples as compare to Xe-360 keV sample. The defects in the Xe-360 KeV samples (which are more towards the surface as predicted by SRIM) might be enough to

hinder the implanted Xe from moving towards the surface. This resulted in the peak shifting towards the bulk. Annealing of more defects at 1200 °C caused implanted Xe to shift towards the surface and diffused out. The significant annealing observed after annealing at 1300 °C caused no further diffusion and shift indicating a radiation enhanced diffusion. In the Xe-360 KeV +167 MeV samples, significant radiation annealing occurred after annealing at 1100 °C. This resulted in no detectable Fickean diffusion and peak shift. The loss of implanted Xe without diffusion might be due to visible grain boundaries with crystallites as seen on the SEM images. These grain boundaries increased in numbers as the annealing temperature resulting in more loss of implanted Xe. Therefore, Radiation damage in TiN and its structure play a major role in the migration behaviour of implanted Xe. The influence of structure in the migration of implanted Xe has been reported [13]

7. Conclusions

TiN powder was successfully sintered using SPS at 1900 °C as confirmed by Raman spectroscopy and XPS studies. RS revealed some structural defects (TA, LA and TO) peaks, with a face-centered hexagonal phase, respectively. The XPS results indicated that Ti 2p doublet spin-orbit difference is 6.0 eV, which confirms formation of TiN and not TiO_2. However, sub oxide of TiO_2 was observed which could be attributed to the oxidation of the samples during preparation and storage. SEM showed uniform surface having few pores confirming good densification, which agrees well with the obtained relative density of 98.5%. The samples were then implanted using Xe ions of 360 keV at RT to a fluence of 1.1×10^{16} cm^{-2}, Raman results showed similar peaks as those obtained from the pristine TiN, indicating the sample retains its original properties (no amorphization occurred). In addition, the effects of SHI on the migration behaviour of Xe implanted at RT into sintered TiN was investigated. RS showed co-irradiated

samples produced relatively less structure disorder. After successive annealing at different temperatures there is evidence of healing of retained damage as Xe is released from the TiN. SEM images show a progressive growth of grain boundaries with increase in annealing temperature with crystallites forming along the grain boundaries. These observations are more pronounced on the co-irradiated samples. From the RBS depth profiles it is evident that the migration of Xe in samples is totally different. In the implanted samples the migration of Xe was by trapping and de-trapping of defects at temperatures below 1200 °C and was mainly through grain boundary diffusion at elevated temperatures. On the co-irradiated samples the migration was mainly via fast grain boundary diffusion. This grain boundary diffusion is in agreement with SEM results as it is observed that the grain boundaries were more pronounced on the co-irradiated samples with crystallites forming on along the grain boundaries. Therefore the defects in the co-irradiated samples tends to heal faster.

Acknowledgements

We appreciate the financial supports from the National Research Fund of South Africa. (Grant UID: 107405)

References

[1] Billot P and Barbier D "Very high temperature reactor VHTR, the French Atomic Agency Commission CEA R&D Program," 2nd Interna- tional Topical Meeting on High Temperature Reactor Technology, Baijing, China, 22–24 September 2004.

[2] A technology Roadmap for Generation IV Nuclear Energy Systems, Is-issued by the US DOE Nuclear Energy Research Advisory committee and the Generation IV International Forum, December 2002; http://gen- iv.ne.doe.gov/

[3] Zinkle S J and Was G S 2013 Materials challenges in nuclear energy *Acta Mater*. **61** 735-758

[4] Chauhan A, Litvinov D, de Carlan Y and Aktaa J 2016, Study of the deformation and damage mechanisms of a 9Cr-ODS steel: Microstructure evolution and fracture characteristics *Mater. Sci. Eng*. A **658** 123-134

[5] Streit M, Ingold F 2005, Nitride as nuclear fuel option, *J. Eur. Ceram. Soc*. **25** 2687-2692.

[6] Minato K, Akabori M, Takano M, Arai Y, Nakajima K, Itoh A (2003), Ogawa T, Fabrication of nitride fuels for transmutation of minor actinides, *J. Nucl. Mater*. **320** 18-24.

[7] Meyer M K, Fielding R and Gan J 2007, Fuel development for gas-cooled fast reactors *J. Nucl. Mater*. **371** 281-287

[8] Kuwahara H, Mazaki N, Takahashi M, Watanabe T, Yang X and Aizawa T 2001 Mechanical properties of bulk sintered titanium nitride ceramics *Mater. Sci. Eng*. A **319**–**321** 687-691

[9] Kitiwan M, Ito A and Goto T 2014, Spark plasma sintering of TiN-TiB2 composites *J. Eur. Ceram. Soc*. **34** 197-203

[10] Wang L, Jiang W, Chen L, Yang M and Zhu H 2006, Consolidation of Nano-Sized TiN Powders by Spark Plasm a Sintering. *J. Am. Ceram. Soc* **2366** 2364-2366

[11] Holleck H 1986, Material selection for hard coatings. *J. Vac. Sci. Technol*. A **4** 2661-2669.

[12] Lengauer W 1992, Properties of bulk δ-TiN_{1-x} prepared by nitrogen diffusion into titanium metal. *J Alloys Compd*. **186** 293-307.

[13] Bes R, Millard-Pinard N, Gavarini S, Cardinal S, Garnier V, Khodja H, Malchère A, Martin P and Peaucelle C 2010 Study of xenon thermal migration in sintered titanium nitride using

nuclear micro-probe *Nucl. Instrum. Methods Phys. Res. Sect. B Beam Interact. with Mater. Atoms* **268** 1880-1883

[14] Groza J R, Curtis J P, Kramer M 2000, Field assisted sintered of nano crystalline titanium nitride, *J. Am. Ceram. Soc*. **83** 1281-1283.

[15] Angerer P, Yu L G, Khor K A, Korb G, Zalite I 2005, Spark plasma-sintering of nano structured titanium carbinitride powders, *J. Eur. Ceram. Soc*. **25** 1919-1927.

[16] Zgalat-Lozynskyy O, Herrmann M, Ragulya A, Andrzejczuk M and Polotai A 2012 Structure and mechanical properties of spark plasma sintered TiN-Based nanocomposites *Arch. Metall. Mater*. **57** 853-858

[17] Ryu H J, Lee Y W, Cha S I and Hong S H 2006, Sintering behaviour and microstructures of carbides and nitrides for the inert matrix fuel by spark plasma sintering *J. Nucl. Mater*. **352** 341-348

[18] Jaeger R E and Egerton L 1962, Hot pressing of pottasium-sodium niobates *J. Am. Ceram. So c*. **45** 209-213

[19] Panda S S, Singh V, Upadhyaya, Agrawal, 2006 Sintering response of austenitic (316L) and ferritic (434L) stainless steel consolidated in conventional and microwave furnaces *Scripta Mater.* **54** 2179-2183

[20] Fleischer R L, Price B P and Walker R M 1975, Nuclear Tracks in Solid: Principles and Applications (Berkeley, Calif., University of California Press)

[21] Hlatshwayo T T, O'Connell J H, Skuratov V A, Msimanga M, Kuhudzai R J, Njoroge E G and Malherbe J B 2015, Effect of Xe ion (167 MeV) irradiation on polycrystalline SiC implanted with Kr and Xe at room temperature *J. Phys. D. Appl. Phys*. **48** 1-7

[22] Ogarkov A I, Shevtsov S V, Kuznetsov K B, Kovalev I A, Chernyavskii A S and Solntsev K A 2016, Irradiation of Titanium, Zirconium, and Hafnium Nitrides with High-Energy Ions *Inorg. Mater*. **52** 561-565

[23] Xue J X, Zhang G J, Guo L P, Zhang H B, Wang X G, Zou J, Peng S M and Long X G 2014, Improved radiation damage tolerance of titanium nitride ceramics by introduction of vacancy defects *J. Eur. Ceram. Soc.* **34** 633-639

[24] Gavarini S, Toulhoat N, Peaucelle C, Martin P, Mende J, Pipon Y and Jaffrezic H 2007 Xenon migration behaviour in titanium nitride *J. Nucl. Mater*. **362** 364-373

[25] Bès R, Gaillard C, Millard-Pinard N, Gavarini S, Martin P, Cardinal S, Esnouf C, Malchère A and Perrat-Mabilon A 2013, Xenon behavior in TiN : A coupled XAS / TEM study *J. Nucl. Mater.* **434** 56-64

[26] Chen C C, Liang X T, Tse W S, Chen I Y and Duh J G 1994, Raman Spectra of Titanium Nitride Thin Films *Chinese J. Phys*. **32** 205-210

[27] Barshilia H C and Rajam K S 2004, Raman spectroscopy studies on the thermal stability of TiN, CrN, TiAIN coatings and nanolayered TiN/CrN, TiAIN/CrN multilayer coatings *J. Mater. Res.* **19** 3196-3205

[28] Rahman M M, Jiang Z T, Munroe P, Chuah L S, Zhou Z, Xie Z, Yin C Y, Ibrahim K, Amri A, Kabir H, Haque M M, Mondinos N, Altarawneh M and Dlugogorski B Z 2016, Chemical

bonding states and solar selective characteristics of unbalanced magnetron sputtered $Ti_x M_{1-x-y} N_y$ films *RSC Adv*. **6** 36373-36383

[29] Cheng Y and Zheng Y F 2007, Characterization of TiN, TiC and TiCN coatings on Ti – 50 . 6 at.% Ni alloy deposited by PIII and deposition technique *Surf. Coat. Technol*. **201** 4909–4912

[30] Han Y, Yue X, Jin Y, Huang X and Shen P K 2016, Hydrogen evolution reaction in acidic media on single-crystalline titanium nitride nanowires as an efficient non-noble metal electrocatalyst *J. Mater. Chem. A* **4** 3673-3677

[31] Bertóti I, Mohai M, Sullivan J L and Saied S O 1995, Surface characterisation of plasma-nitrided titanium: an XPS study *Appl. Surf. Sci*. **84** 357-371

[32] Greczynski G and Hultman L 2017, C 1s Peak of Adventitious Carbon Aligns to the Vacuum Level : Dire Consequences for Material's Bonding Assignment by Photoelectron Spectroscopy *chemphychem Commun*. **18** 1–7

[33] Jiao L (PhD Thesis 2015), Enhanced Radiation Tolerance of Ceramic Thin Films by Nano-structural Design (Texas A&M University) pages 45-48

[34] Ziegler J F and Biersack J 2010 SRIM 2010, The stopping and range of ions in matter *Nucl. Instrum. Methods Phys. Res. B* **268** 1818–1823